Control of nanostructures by cooling rate in spinel-type manganese oxide $ZnMnGaO_4$

M. Ishimatsu[1], H. Tabuki[1], and Y. Horibe[1,2]*

[1]*Department of Materials Science and Engineering, Kyushu Institute of Technology, 1-1 Sensui-cho, Tobata-ku, Kitakyushu, Fukuoka 804-8550, Japan*

[2]*Research Center for Neuromorphic AI Hardware, Kyushu Institute of Technology, 2-4 Hibikino, Wakamatsu-ku, Kitakyushu, Fukuoka 808-0196, Japan*

*Email address: horibe@post.matsc.kyutech.ac.jp

Abstract

Controllability of the nanostructures in spinel-type manganese oxide $ZnMnGaO_4$ by changing cooling rate was studied via transmission electron microscopy (with selected area electron diffraction and bright- and dark-field imaging) as well as X-ray diffraction. The Quench sample exhibited a tweed pattern, suggesting the coexistence of two phases at the nanometer scale. The nanostructural changes from a fine twin structure to a checkerboard nanostructure, followed by the emergence of a lamellar-type nanostructure, were clearly observed as the cooling rate decreased from quenching to 1 °C/h. It was suggested that the diffusion of manganese ions accompanied by the Jahn–Teller distortion play an important role in the formation of nanostructures of this system.

1. Introduction

Self-assembled materials based on phase separation have been extensively fabricated to improve the physical properties of materials [1–11]. In particular, self-assembled nanostructures of transition metal oxides have received significant interest in the areas of ceramics and thin films, owing to their potential applicability [12–23]. Self-assembled checkerboard (CB)-type nanostructures of spinel-type manganese oxides, owing to the nanoscale phase separation related to Mn^{3+} ions accompanied by the Jahn–Teller distortion, are some of the well-known examples [24-26]. For example, the formation of a CB-type nanostructure was observed for 10 °C/h slow-cooled $Mg(Mn, Fe)_3O_4$ [27]. $(Co, Mn, Fe)_3O_4$ was also studied for the formation and growth of CB- and lamellar-type nanostructures under isothermal annealing at 375 °C [28,29]. The CB-type nanostructures were found to consist of highly anisotropic and well-ordered nanorods: two types of Mn-poor cubic and two types of Mn-rich tetragonal nanorods. Furthermore, it was reported that further increasing the annealing time changed the CB-type nanostructures of $(Co, Mn, Fe)_3O_4$ to lamellar-type nanostructures [30]. This formation of thermally induced nanostructures of $(Co, Mn, Fe)_3O_4$ drastically changed its magnetic properties, such as coercivity [28–30]. A mixed system of $ZnGa_2O_4$ and $ZnMn_2O_4$, $ZnMnGaO_4$, under a low cooling rate of 5 °C/h also presented a CB-type nanostructure consisting of highly anisotropic nanorods of ~4 nm × 4 nm × 70 nm in size [24]. However, the change in the CB-type nanostructure of $ZnMnGaO_4$ by controlling the annealing conditions still remains unclear.

$ZnGa_2O_4$ phosphor has recently been studied as a potential candidate for field emission displays and plasma display panels [31–35]. In particular, as photocatalysts, $ZnGa_2O_4$ nanoparticles have been found to present hydrolytic hydrogen generation activity, and their synthesis has been attempted by various methods, such precipitation and solution combination methods [36,37]. Therefore, the fabrication of nanomaterials containing $ZnGa_2O_4$ and control of their dimensions will be of interest.

In this study, we investigated the change in the nanostructures of spinel-type manganese oxide $ZnMnGaO_4$ as a function of the cooling rate from a high temperature via X-ray diffraction and transmission electron microscopy (TEM). A tweed pattern observed in the quenched sample was found to change to a nano-twin structure under a low cooling rate of 120 °C/h, followed by the formation of a CB-type nanostructure under 5 °C/h cooling, as reported in a previous research [24]. Furthermore, a lower cooling rate of 1 °C/h resulted in the evolution of a lamellar-type nanostructure. These results indicated that the cooling rate plays an important role in the formation of nanostructures of $ZnMnGaO_4$, suggesting the importance of the diffusion of manganese ions accompanied by the Jahn–Teller distortion in this system.

2. Methods

$ZnMnGaO_4$ polycrystalline samples were prepared in air by a conventional solid-state reaction method. A mixture of ZnO, Mn_2O_3, and Ga_2O_3 powders was pelletized and calcined at 950 °C for 5 h, followed by calcination at 1000 °C for 15 h. After the final sintering at 1150 °C for 24 h, the samples were quenched or cooled to room temperature with different cooling rates of 120 °C/h, 5 °C/h, and 1 °C/h, respectively. The macroscopic crystal structure was studied using a powder X-ray diffractometer (Rigaku SmartLab). The TEM observations were conducted using a JEM-3000F (acceleration voltage: 300 kV) transmission electron microscope at room temperature. All reflection peaks and spots in the X-ray and electron diffraction patterns are indexed based on the cubic spinel structure.

3. Results and discussion

The macroscopic crystal structure of $ZnMnGaO_4$ recorded by powder X-ray diffraction revealed the dependence of the evolution of nanostructures on the cooling rate. Figure 1 shows the X-ray diffraction profiles near the 311 reflection peak for the samples

quenched and cooled to room temperature with the rates of 120 °C/h, 5 °C/h, and 1 °C/h, respectively. The diffraction profiles obtained for both the quenched (Quench) and 120 °C/h-cooled samples present a remarkable peak splitting resulting from the tetragonal spinel structure, namely, the 311 peak (in cubic notation) splits into the 310_t and 211_t peaks (where the subscript "T" represents the indices base on the tetragonal spinel structure). However, the 120 °C/h-cooled sample exhibits a comparatively larger splitting, with the 311 peak shifting toward a higher 2θ scattering angle. The dependence of the lattice parameters on the cooling rate estimated from these profiles is summarized in Table 1. The tetragonal lattice parameters of Quench and the 120 °C/h-cooled sample are ($a_{T'/Quench}$ ~8.30 Å and $c_{T'/Quench}$ ~8.58 Å) and ($a_{T'/120\,°C}$ ~8.21 Å and $c_{T'/120\,°C}$ ~8.74 Å), respectively, indicating the evolution of tetragonality under slow cooling. It is noted that only the tetragonal phase, the so-called T' phase [24–28], is detected in the powder X-ray diffraction patterns of both the samples within experimental uncertainties. As the cooling rate is decreased, the separation of the peak splitting increases, followed by drastic changes in the X-ray diffraction profiles, as observed for the 5 °C/h-cooled sample. The X-ray diffraction profiles of both the 5 °C/h- and 1 °C/h-cooled samples in Fig. 1 can be indexed by the superposition of cubic $ZnGa_2O_4$ (space group: $Fd\bar{3}m$, denoted by C) and tetragonal $ZnMn_2O_4$ (space group: $I4_1/amd$, denoted by T), suggesting the coexistence of these phases. The lattice parameters obtained from these profiles for C and T are C: $a_{C/5\,°C}$ ~8.30 Å and T: $a_{T/5\,°C}$ ~8.11 Å, $c_{T/5\,°C}$ ~9.10 Å for the 5 °C/h-cooled sample and C: $a_{C/1\,°C}$ ~8.31 Å and T: $a_{T/1\,°C}$ ~8.11 Å, $c_{T/1\,°C}$ ~9.15 Å for the 1 °C/h-cooled sample. These parameters are similar to those of $ZnGa_2O_4$ (a ~8.33 Å) [38] and tetragonal $ZnMn_2O_4$ (a ~8.09 Å, c ~9.24 Å) [39]. Furthermore, the diffraction peaks of the 5 °C/h- and 1 °C/h-cooled samples are significantly broadened, owing to the formation of nanostructures. These results suggest that in the present system, low cooling rates lead to structural phase separation of $ZnMnGaO_4$ into Mn-rich tetragonal and Mn-poor cubic phases with the formation of nanostructures. In comparison, high cooling rates result in a single

tetragonal phase, probably owing to the Jahn–Teller distortion.

Electron diffraction observations via TEM revealed the characteristic changes occurring with the cooling rate. The electron diffraction patterns obtained for the samples at different cooling rates are shown in Figs. 2(a)–(d), respectively. The diffraction pattern for Quench (Fig. 2(a)) presents remarkable diffused streaks along the [110] and [$1\bar{1}0$] directions around the fundamental spots, which are due to the local lattice distortions within the sample. In the pattern obtained from the 120 °C/h-cooled sample (Fig. 2(b)), there is a remarkable splitting of the diffraction spots along the [$1\bar{1}0$] direction. The emergence of a twin structure is indicated by the large splitting of the spots in the high-scattering-angle reciprocal region as well as by the absence of splitting along the [$1\bar{1}0$] direction through origin 000. However, for the sample cooled at the rate of 5 °C/h (Fig. 2(c)), anomalous splitting of the diffraction spots is observed in the electron diffraction pattern; for example, the reflection spots of the *h00* series split into four branches along the [100] and [010] directions. These characteristic diffraction patterns are almost identical to those found for CB-type nanostructures, as reported previously [24,29,30,40,41]. This suggests the presence of two types of tetragonal nanorods with different directions of the tetragonal long-axis (indicated by α and γ near the 800-reciprocal position) and two types of cubic nanorods with different directions of the unit cell rotation (indicated by β and δ near the 800-reciprocal position). Annealing at a lower cooling rate of 1 °C/h leads to the splitting of the diffraction spots along only the [$1\bar{1}0$] direction, as shown in Fig. 2(d). It should be noted that regardless of the similarity between Figs. 2(b) and (d), the diffraction spot denoted by C in Fig. 2(d) is located at the positions expected from the cubic structure without lattice distortions. The splitting of these diffraction spots is similar to that reported in $(Co, Mn, Fe)_3O_4$ [30], indicating the coexistence of cubic and tetragonal domains in the 1 °C/h-cooled sample. The electron diffraction pattern depicted in Fig. 2(d) reveals that the unit cells of the cubic phase are rotated by ~3.0° relative to those of the tetragonal structures, in excellent agreement with the value estimated, ~3.4°,

from simple geographical calculations of the X-ray diffraction.

The morphological features associated with these electron diffraction patterns are remarkably demonstrated in the corresponding dark- and bright-field images, as schematically shown in Figs. 3(a)–(d). The images in Figs. 3(a)–3(d) were taken using the 400, $2\bar{2}0$, 400, and 000 diffraction spots (transmitted electrons), respectively. Dark-field images taken for Quench (Fig. 3(a)) reveal a tweed pattern in the sample, suggesting a fine dispersion of the cubic phase in the matrix. In this case, the presence of the tweed pattern suggests a local occurrence of cubic regions in the tetragonal matrix, prior to the phase separation associated with the Jahn–Teller strain due to Mn^{3+} ions. It is noted that large-sized twin domains are observed in Quench. In comparison, very fine twins with a width of ~15 nm are observed in the dark-field image obtained for the 120 °C/h-cooled sample (Fig. 3(b)). The appearance of nanotwins can be attributed to the uniform Jahn–Teller strain associated with Mn^{3+} randomly present in the sample, resulting in an averaged tetragonal crystal structure accompanied by large tetragonalities. Note that phase transitions from cubic to tetragonal structures are frequently accompanied by strain-relieving twinning. Similar to previous reports, highly ordered CB-type nanostructures are found in the dark-field images (Fig. 3(c)) obtained for the 5 °C/h-cooled sample [24]. The typical size of the domains is ~7 nm × 7 nm. The inset exhibits the schematic figure corresponding to the region framed in Fig. 3(c). Along with herringbone-type patterns with a typical length of approximately 130 nm in the sideview observations (not shown here), the CB-type nanostructures consist of two types of tetragonal nanorods (α and γ) and two types of cubic nanorods (β and δ), which are highly ordered along the [110] and $[1\bar{1}0]$ directions. It should be mentioned that the TEM image showing the CB-type nanostructures is a projection from the [001] direction. Interestingly, in the 1 °C/h-cooled sample, band-like domains with a width of ~35 nm can be clearly observed in the bright-field image (Fig. 3(d)), which is similar to Fig. 3(b). However, the band-like domains are of two distinct types: with parallel boundaries and with

an inclination of ~22°, in good agreement with the value of ~26° suggested by a simple estimation from the differences between the lattice parameters of the cubic and tetragonal cells. The different directions of the domain boundaries in Fig. 3(d) as well as the characteristic splitting of the diffraction spots shown in the electron diffraction pattern in Fig. 2(d) demonstrate the appearance of lamellar-type nanostructures. These nanostructures consist of one type of cubic nanoplates and two types of tetragonal nanoplates with different orientations of the tetragonal long axes in the 1 °C/h-cooled sample, similar to those reported for $(Co, Mn, Fe)_3O_4$ [29,30]. It should be mentioned that the electron diffraction pattern of Fig. 2(d) was taken from the region framed by the circle in Fig. 3(d) consisting of the cubic nanoplate and only one type of the tetragonal nanoplate. Whereas the other electron diffraction patterns were obtained from the whole regions in Fig. 3(a) - Fig. 3(c). Therefore, based on the results of annealing at different cooling rates from temperatures above which the chemical phase separation occurs, there is a morphological change from the tweed structure to the nano-twins, followed by formation of nano-CB and lamellar-type nanostructures, with the corresponding crystallographic changes. We would like to emphasize that these morphological changes in the $ZnMnGaO_4$ system that depend on the cooling rate are very similar to the nanostructural changes in $(Co, Mn, Fe)_3O_4$ when it is isothermally annealed for different times [28,30].

Summarizing, nanostructural change from tweed patterns to lamellar-type nanostructures related to nanoscale phase separation were observed in the samples cooled down to room temperature with different cooling rates. Higher cooling rates led to a nanostructural change to the tweed pattern or nanotwin structure, whereas lower cooling rates resulted in the appearance of the lamellar-type nanostructures, with the CB-type nanostructures as the intermediate states. Figures 4(a) and (b) depict three-dimensional schematics of the CB- and lamellar-type nanostructures, respectively. A CB pattern can be observed in the cross-section of the aggregate texture of the nanorods, *i.e.*, two types of cubic

nanorods with different rotation directions of the unit cells and two types of tetragonal nanorods with different directions of tetragonality, perpendicular to the [001] direction. In comparison, a lamellar pattern can be seen in the cross-sectional view of the aggregate texture of the nanoplates, *i.e.*, one type of cubic nanoplate and two types of tetragonal nanoplates with different directions of tetragonality, perpendicular to the [001] direction. It should be noted that the cross-sections perpendicular to the lateral direction (i.e., the [100] and [010] directions) indicate the so-called herringbone nanostructures, in both the cases [24,28], suggesting that these nanostructures cannot be distinguished from the TEM images when viewed from the lateral directions. The origins of these interesting nanostructures are schematically illustrated in Figs. 4(c) and (d). The CB-type nanostructure comprises four different types of nanorods: two types of cubic nanorods and two types of tetragonal nanorods. As discussed in previous reports, it is suggested that the CB-type nanostructures relax the elastic strain efficiently on the nanometer scale and acquire the energy of the entire system by a subtle arrangement of these four types of nanorods [24,27,30]. However, they cannot maintain their stability when the nanorods become larger, and thus, lamellar nanostructures presumably form in this system [30]. Specifically, a lower cooling rate to reach room temperature leads to the evolution of nanostructures, resulting in a lamellar-type nanostructure that consists of two types of tetragonal nanoplates and one type of cubic nanoplates. Indeed, as shown in Fig. 4(d), the boundaries between the cubic and tetragonal nanoplates are analogous to strain-relieving twin boundaries.

Figures 4(e) and (f) depict the schematics of the relative rotations of the cubic and tetragonal unit cells across the boundary in the CB- and lamellar-type nanostructures, respectively. To compensate for the tetragonal distortions at the tetragonal–cubic boundary, the tetragonal unit cells are suggested to be rotated by ~3.3° and ~ 3.4° in the CB- and lamellar-type nanostructures, respectively. Interestingly, their rotation angles are very similar to each other, regardless of their very different morphological features. For $(Co, Mn, Fe)_3O_4$,

both the CB- and lamellar-type nanostructures fabricated by different isothermal annealing hours are reported to be accompanied by almost identical local structures near the tetragonal–cubic boundary, suggesting that the sizes of the domains play crucial roles in nanostructure formation [30]. Consequently, the morphological differences in the $ZnMnGaO_4$ samples annealed with different cooling rates originate from the distinct sizes of the CB- and lamellar-type nanostructures, owing to the evolution of the phase separations induced by the manganese ion diffusion accompanied by the Jahn–Teller strain at the nanometer scale. Specifically, the nanostructural changes in this system associated with the difference in the cooling rates are suggested to be caused by the evolution of the domains due to strain relaxation at the nanometer scale.

4. Conclusions

In conclusion, we investigated the cooling rate dependence of the nanostructural changes in spinel-type manganese oxide $ZnMnGaO_4$ by X-ray diffraction and TEM. In Quench, a tweed texture was observed, indicating the coexistence of two phases at the nanometer scale. The nanostructures changed from nano-twins to CB-type and lamellar-type nanostructures with the decrease in the cooling rate. Our TEM studies clearly demonstrated that the cooling rate plays an important role in the formation of nanostructures of $ZnMnGaO_4$, suggesting the importance of the diffusion of the manganese ions accompanied by the Jahn–Teller distortion in this system.

Acknowledgements

The authors would like to thank Prof. M. Ishimaru and Dr. H. -J. Woo for the experimental supports and the useful discussions. The X-ray diffraction measurements in this study were performed in Center for Instrumental Analysis (CIA), Kyushu Institute of Technology.

References

[1] Y. Le Bouar, A. Loiseau, and A. G. Khachaturyan, Acta Mater. **46**, 2777 (1998).

[2] S. Sun, C. B. Murray, D. Weller, L. Folks, and A. Moser, Science **287**, 1989 (2000).

[3] O. Rathore and D. Y. Sogah, J. Am. Chem. Soc. **123**, 5231 (2001).

[4] Z. L. Xiao, C. Y. Han, U. Welp, H. H. Wang, W. K. Kwok, G. A. Willing, J. M. Hiller, R. E. Cook, D. J. Miller, and G. W. Crabtree, Nano Lett. **2**, 1293 (2002).

[5] F. X. Redl, K.-S. Cho, C. B. Murray, and S. O'Brien, Nature **423**, 968 (2003).

[6] H. Zheng, J. Wang, S. E. Lofland, Z. Ma, L. Mohaddes-Ardabili, T. Zhao, L. Salamanca-Riba, S. R. Shinde, S. B. Ogale, F. Bai, D. Viehland, Y. Jia, D. G. Schlom, M. Wuttig, A. Roytburd and R. Ramesh, Science. **303**, 661 (2004).

[7] Y. Lin, A. Boker, J. He, K. Sill, H. Xiang, C. Abetz, X. Li, J. Wang, T. Emrick, S. Long, Q. Wang, A. Balazs, and T. P. Russell, Nature **434**, 55 (2005).

[8] A. Suzuki and M. Takeyama, J. Mater. Res. **21**, 21 (2006).

[9] J. Yang, H. I. Elim, Q. Zhang, J. Y. Lee, and W. Ji, J. Am. Chem. Soc. **128**, 1192 (2006).

[10] J. Huang, Y. Wu, C. Gu, M. Zhai, K. Yu, M. Yang, and J. Liu, Sens. Actuators B Chem. **146**, 206 (2010)

[11] L. Zhou, M. K. Miller, P. Lu, L. Ke, R. Skomski, H. Dillon, Q. Xing, A. Palasyuk, M. R. McCartney, D. J. Smith, S. Constantinides, R. W. McCallum, I. E Anderson, V. Antropov and M. J. Kramer, Acta Mater. **74**, 224 (2014).

[12] S. Aggarwal, A. P. Monga, S. R. Perusse, R. Ramesh, V. Ballarotto, E. D. Williams, B. R. Chalamala, Y. Wei, and R. H. Reuss, Science **287**, 2235 (2000).

[13] J. L. MacManus-Driscoll, S. R. Foltyn, Q. X. Jia, H. Wang, A. Serquis, L. Civale, B. Maiorov, M. E. Hawley, M. P. Maley, and D. E. Peterson, Nat. Mater. **3**, 439 (2004).

[14] B. S. Guiton and P. K. Davies, Nat. Mater. **6**, 586 (2007).

[15] B. S. Guiton and P. K. Davies, J. Am. Chem. Soc. **130**, 17168 (2008).

[16] V. Polshettiwar, B. Baruwati, and R. S. Varma, ACS Nano **3**, 728 (2009).

[17] L. Pálová, P. Chandra, and K. M. Rabe, Phys. Rev. **B82**, 075432 (2010)

[18] M. W. Licurse, and P. K. Davies, Appl. Phys. Lett. **97**, 123101 (2010).

[19] A. Chen, Z. Bi, H. Hazariwala, X. Zhang, Q. Su, L. Chen, Q. Jia, J. L. MacManus-Driscoll and H. Wang, Nanotechnol. **22**, 315712 (2011).

[20] A. Chen, Z. Bi, Q. Jia, J. L. MacManus-Driscoll and H. Wang, Acta Mater. **61**, 2783 (2013).

[21] X. Li, J. Wei, Q. Li, S. Zheng, Y. Xu, P. Du, C. Chen, J. Zhao, H. Xue, Q. Xu, and H. Pang, Adv. Funct. Mater. **28**, 1800886 (2018).

[22] M. Zheng, H. Tang, L. Li, Q. Hu, L. Zhang, H. Xue, and H. Pang, Adv. Sci. **5**, 1700592 (2018)

[23] A. Chen, Q. Su, H. Han, E. Enriquez and Q. Jia, Adv. Mater. **31**, 1803241 (2019).

[24] S. Yeo, Y. Horibe, S. Mori, C. M. Tseng, C. H. Chen, A. G. Khachatuyan, C. L. Zhang and S. –W. Cheong, Appl. Phys. Lett. **89**, 233120 (2006).

[25] A. Kosuga, K. Kurosaki, K. Yubuta, A. Charoenphakdee, S. Yamanaka, and R. Funahashi, J. Electron. Mater. **38**, 1303 (2009).

[26] K. Koumoto, Y. Wang, R. Zhang, A. Kosuga, and R. Funahashi, Annu. Rev. Mater. Res. **40**, 363 (2010).

[27] C. L. Zhang, S. Yeo, Y. Horibe, Y. J. Choi, S. Guha, M. Croft, S. –W. Cheong and S. Mori, Appl. Phys. Lett. **90**, 133123, (2007).

[28] C. L. Zhang, C. M. Tseng, C. H. Chen, S. Yeo, Y. J. Choi, and S.-W. Cheong, Appl. Phys. Lett. **91**, 233110 (2007).

[29] M. Ohno, S. Mori, Y. Togawa and Y. Horibe, IOP Conf. Ser.: Mater. Sci. Eng. **18**, 092052 (2011).

[30] Y. Horibe, M. Ishimatsu, S. Takeyama, S. Mori, M. Kudo, M. Auchi and Y. Murakami, Appl. Phys. Lett. **115**, 232401, (2019).

[31] K.-H. Hsu, M.-R. Yang, and K -S. Chen, J. Mater. Sci. Mater. El. **9**, 283 (1998).

[32] S. Park , Y. –J. Chung , J. C. Lee , K. Yoo, B. –W. Kim, and J. –H. Lee, J Electroceram. **17**, 827 (2006).

[33] J. H. Cha and H. W. Choi, Trans. Electr, Electron. Mater. **12**, 11 (2011).

[34] Q. Huo, W. Tu, and L. Guo, Opt. Mater. **72**, 305 (2017).

[35] C. R. Garcia, J. Oliva, L. A. Diaz-Torres, E. Montes, G. Hirata, J. Bernal-Alvarado, and C. Gomez-Solis, Ceram. Int. **45**, 4972 (2019).

[36] Y. Sakata, Y. Matsuda, T. Yanagida, K. Hirata, H. Imamura and K. Teramura, Catal Lett. **125**, 22 (2008).

[37] K. –W. Chang and J. –J. Wu, J. Phys. Chem. B. **109**, 13572 (2005).

[38] J. Hornstra and E. Keulen, Philips Research Reports **27**, 76 (1972).

[39] M. Nogues and P. Poix, J. Phys. Chem. Solids **23**, 711 (1962).

[40] S. Park, Y. Horibe, T. Asada, L. S. Wielinski, N. Lee, P. L. Bonanno, S. M. O'Malley, A. A. Sirenko, A. Kazimirov, M. Tanimura, T. Gustafsson, and S. -W. Cheong, Nano Lett. **8**, 720 (2008).

[41] Y. Horibe, S. Takeyama, and S. Mori, AIP Conf. Proc. **1763**, 050005 (2016).

Figure captions:

Fig. 1. (Color Online)

X-ray powder diffraction profiles of $ZnMnGaO_4$ samples cooled down to room temperature with different cooling rates. C and T indicate 2θ positions of diffraction peaks in cubic spinel $ZnGa_2O_4$ and tetragonal spinel $ZnMn_2O_4$, respectively.

Fig. 2. (Color Online)

Electron diffraction patterns obtained for samples of $ZnMnGaO_4$ with the cooling rates of (a) Quench, (b) 120 °C/h, (c) 5 °C/h, and (d) 1 °C/h, respectively. Electron incidences are almost parallel to [001] direction.

Fig. 3. (Color Online)

Nanostructural changes in $ZnMnGaO_4$ depending on cooling rate: (a) Quench, (b) 120 °C/h, (c) 5 °C/h, and (d) 1 °C/h, respectively. Schematics emphasize morphological features in corresponding image at each cooling rate.

Fig. 4. (Color Online)

Schematics of CB - and lamellar-type nanostructures. (a) and (b); three-dimensional schematics of the CB- and lamellar-type nanostructures, respectively. (c) and (d); cross-sectional schematics of the CB - and lamellar-type nanostructures from the top view direction. (e) and (f); enlarged views near the cubic–tetragonal domain boundaries framed in (c) and (d). Each square in the blue or white regions represents a cubic or a tetragonal unit cell, respectively. Arrows in tetragonal unit cells indicate direction of tetragonal long axes.

Table 1. Dependence of lattice parameters on the cooling rates estimated from X-ray diffraction profiles. T and T' represent tetragonal phase with and without cubic phase as the result of phase separation.

Cooling rates	Phases	Lattice parameters (Å)	
		T / T '	C
Quench	T'	a ~ 8.30	
		c ~ 8.58	
120 °C / h	T'	a ~ 8.21	
		c ~ 8.74	
5 °C / h	T + C	a ~ 8.11	a ~ 8.30
		c ~ 9.10	
1 °C / h	T + C	a ~ 8.11	a ~ 8.31
		c ~ 9.15	

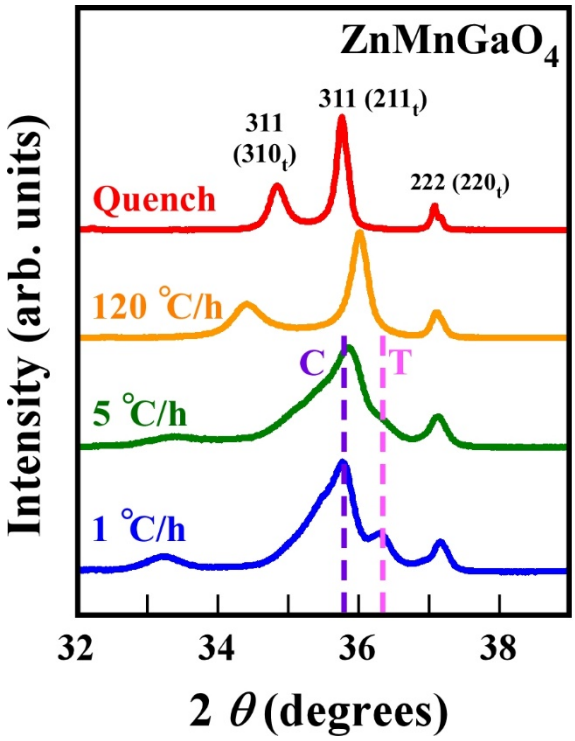
ZnMnGaO4
311 (211t)
311
(310t)
222 (220t)
Quench
120 ℃/h
C
T
5 ℃/h
1 ℃/h
Intensity (arb. units)
32
34
36
38
2 θ (degrees)

Fig. 1

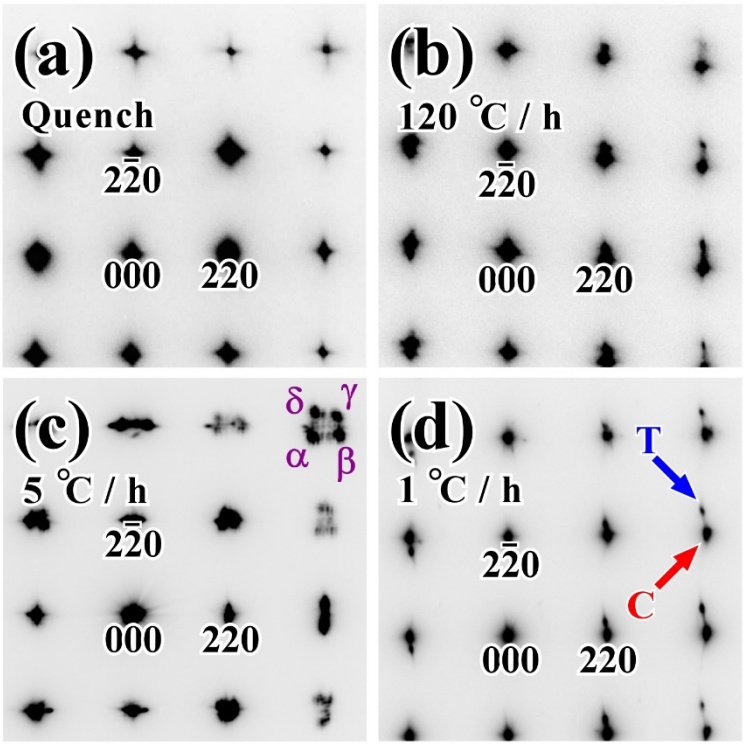
(a)
Quench
2$\bar{2}$0
000
220
(b)
120 °C / h
2$\bar{2}$0
000
220
(c)
5 °C / h
δ
γ
α
β
2$\bar{2}$0
000
220
(d)
1 °C / h
T
C
2$\bar{2}$0
000
220

Fig. 2

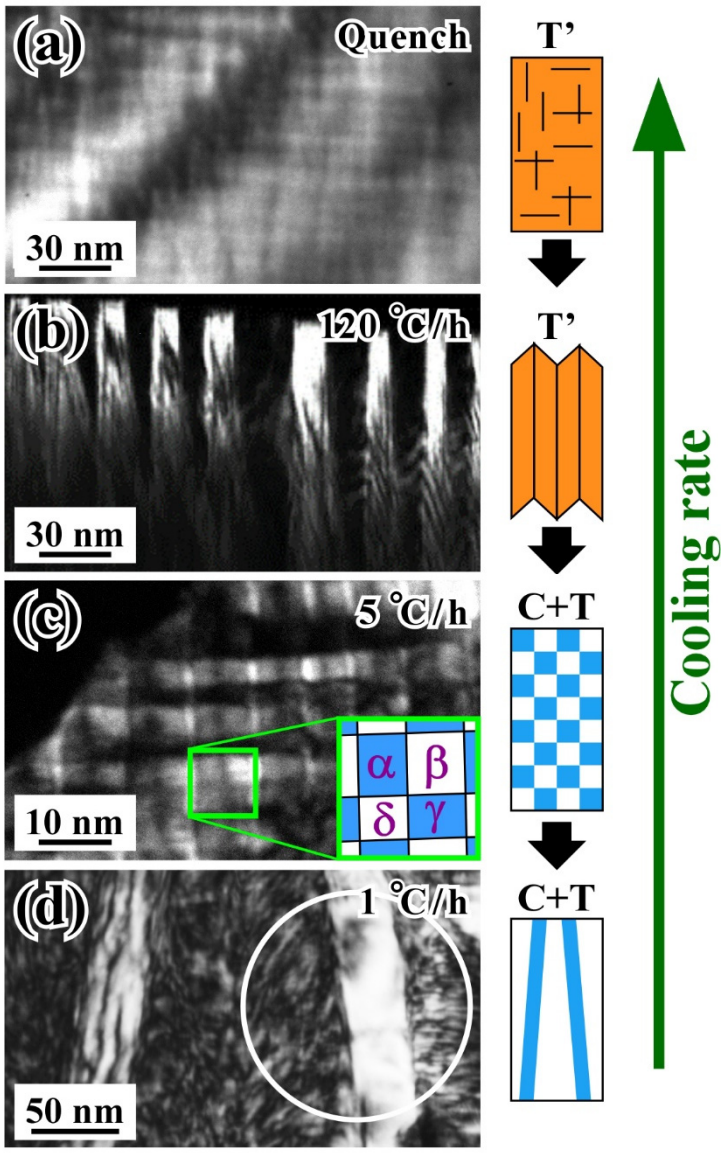
(a)
Quench
30 nm
(b)
120 °C/h
30 nm
(c)
5 °C/h
α
β
δ
γ
10 nm
(d)
1 °C/h
50 nm
T'
T'
C+T
C+T
Cooling rate

Fig. 3

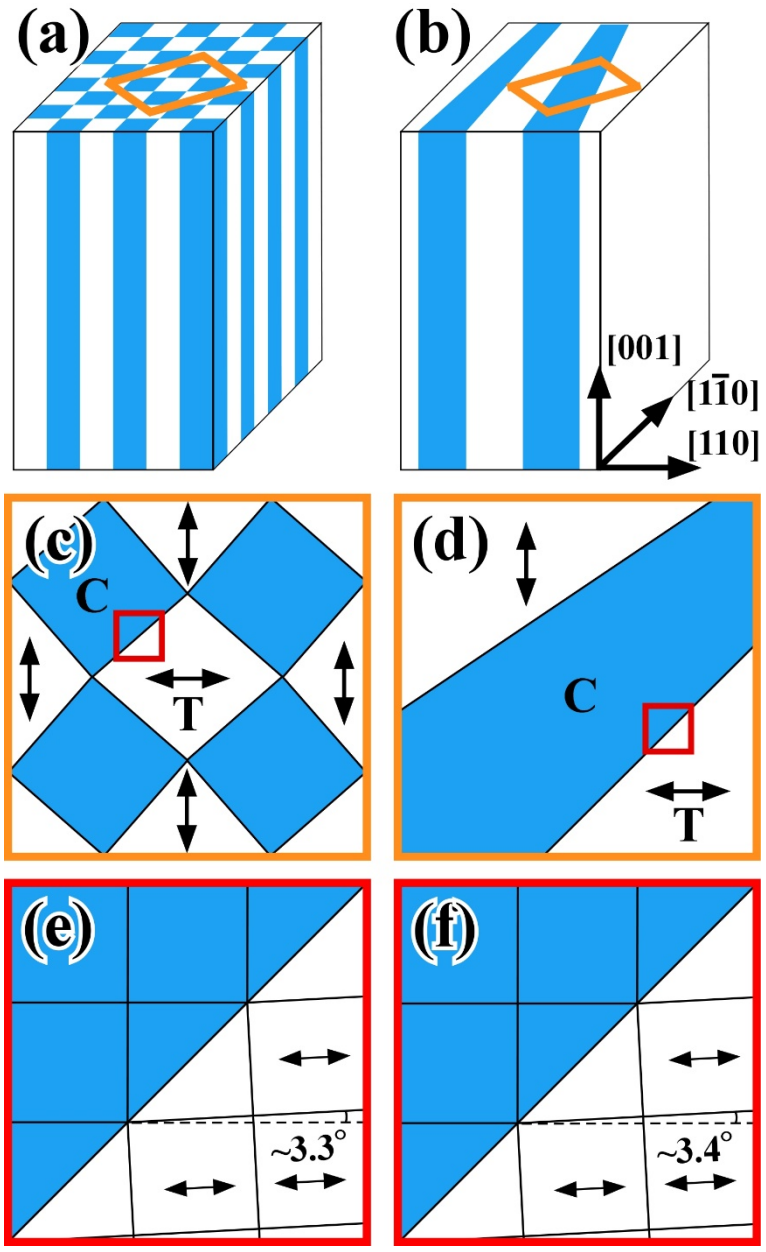

Fig. 4